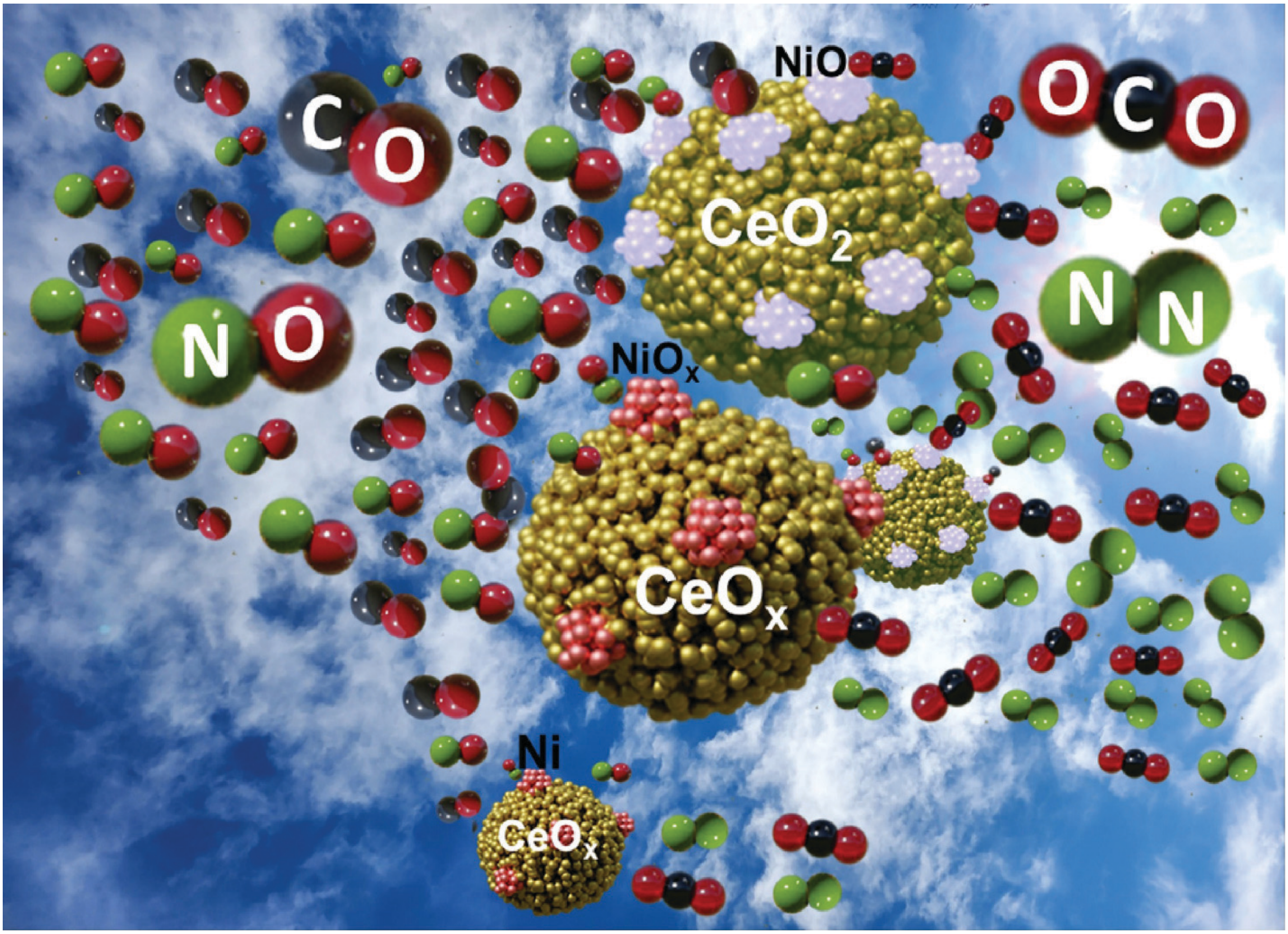

Showcasing research from Kyung-Min Lee, Byeongseok Kim, Juwon Lee, Gihan Kwon, Kwangsuk Yoon, Hocheol Song, Kyung Hoon Min, Sang Eun Shim, Sungwon Hwang, and Taejin Kim's group at Stony Brook University (U.S.A), Inha University (Republic of Korea), Brookhaven National Laboratory (U.S.A), and Hanyang University (Republic of Korea).

The NO reduction by CO over NiO_x/CeO_2 catalysts with a fixed Ni surface density: pretreatment effects on the catalyst structure and catalytic activity

The impact of the physicochemical properties of NiO_x/CeO_2 catalyst-specifically the oxidation state, specific surface area, and defect site-was investigated concerning the fixed Ni surface density (# of Ni atoms/nm^2) on its catalytic performance for NO reduction by CO reaction. This study suggests that Ni oxide, higher specific surface area, and ceria defect sites are advantageous for producing N_2 and CO_2 at lower temperatures.

As featured in:

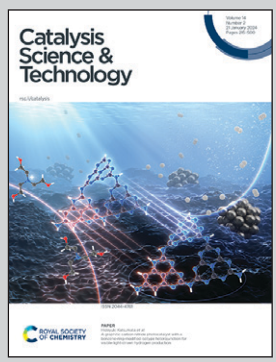

See Taejin Kim *et al.*, *Catal. Sci. Technol.*, 2024, **14**, 279.

Catalysis Science & Technology

ROYAL SOCIETY OF CHEMISTRY

PAPER

View Article Online
View Journal | View Issue

Cite this: *Catal. Sci. Technol.*, 2024, **14**, 279

The NO reduction by CO over NiO_x/CeO_2 catalysts with a fixed Ni surface density: pretreatment effects on the catalyst structure and catalytic activity†

Kyung-Min Lee,‡[a] Byeongseok Kim, ‡[ab] Juwon Lee,[ab] Gihan Kwon, [c] Kwangsuk Yoon, [d] Hocheol Song,[d] Kyung Hoon Min,[b] Sang Eun Shim, [b] Sungwon Hwang[b] and Taejin Kim *[a]

Received 8th August 2023, Accepted 10th November 2023

DOI: 10.1039/d3cy01103h

rsc.li/catalysis

NiO_x/CeO_2 catalysts have shown promising results in various catalytic reactions, including the NO reduction by CO. In this study, we investigated the effect of oxidation and reduction treatments on the NO reduction by CO over pretreated NiO_x/CeO_2 catalysts. A series of oxidized and reduced supported NiO_x catalysts were synthesized in two steps: (1) the pretreatment of CeO_2 supports at different temperatures (400, 500, and 700 °C) under oxidizing and reducing conditions and (2) the synthesis of NiO_x/CeO_2 catalysts by an incipient wetness impregnation method (IWI) with a fixed surface density of 5.3 Ni per nm^2 under specific conditions (oxidation/reduction) applied during the CeO_2 treatment. The prepared catalysts were characterized *via* BET, ICP/OES, Raman, XPS, and XRD to understand their physicochemical properties. The results showed that as the pretreatment temperature increased, the physicochemical properties of NiO_x/CeO_2 catalysts were changed: a decreased specific surface area (SSA), decreased oxygen vacancy/defect sites, and an increased crystallite size. The oxidized NiO_x/CeO_2 catalyst at a lower pretreatment temperature displayed a better catalytic activity, indicating that the physicochemical properties of the catalysts were key factors in enhancing the catalytic activity. To understand the intermediate species and reaction mechanism during the NO reduction by CO, an *in situ* DRIFTS study was performed and a possible reaction mechanism was also discussed.

1. Introduction

Bulk and supported nickel oxide (NiO_x) or nickel (Ni) catalysts have been applied to diverse chemical reactions (*e.g.*, CO-PROX,[1] HER,[2] selective hydrazine decomposition,[3] CO oxidation,[4] methanol steam reforming,[5] dry reforming,[6] and NO reduction by CO[7–11]) owing to their low cost and high activity. It has been reported that the particle size and morphologies of Ni are related to the catalytic performance, such as the decomposition of methane into H_2 and carbon nanofilaments.[12] In addition to surface Ni species, support materials can also influence the reactant activation, stability, and selectivity. Among several support materials, ceria (CeO_2) or CeO_2-based materials have been extensively used because of the easy generation of oxygen vacancies, a high oxygen mobility, and a strong oxygen storage/release capacity (OSC) in the redox cycle (Ce^{3+}/Ce^{4+}).[13–15] Y. Wang *et al.* reported that NiO/CeO_2 catalysts exhibited a higher catalytic activity for the NO reduction by CO than NiO/γ-Al_2O3 and NiO/TiO_2 catalysts due to the synergetic effect of nickel and ceria, resulting from easily reduced oxygen species on the NiO/CeO_2 surface.[7] I. Iglesias *et al.* compared Ni/CeO_2 and $Ni/Ce_{0.85}Zr_{0.15}O_2$ catalysts to understand the effect of Zr on the catalytic property for CO_2 methanation reaction.[16] The authors concluded that $Ni/Ce_{0.85}Zr_{0.15}O_2$ catalysts showed a higher activity and stability than Ni/CeO_2 owing to the higher oxygen mobility, surface species reducibility, and Ni dispersion. In previous studies, we reported that the loading of NiO_x and pretreatment conditions can affect the physicochemical properties (*i.e.*, the specific surface area (SSA), crystallite size,

[a] Materials Science and Chemical Engineering Department, Stony Brook University, Stony Brook, NY, 11794, USA. E-mail: taejin.kim@stonybrook.edu
[b] Department of Chemistry and Chemical Engineering, Education and Research Center for Smart Energy and Materials, Inha University, Incheon, 22212, South Korea
[c] National Synchrotron Light Source II, Brookhaven National Laboratory, Upton, NY 11973, USA
[d] Department of Earth Resources and Environmental Engineering, Hanyang University, Seoul 04763, Republic of Korea

† Electronic supplementary information (ESI) available. See DOI: **https://doi.org/10.1039/d3cy01103h**
‡ Co-first author.

and defect sites) of NiO_x/CeO_2 and the catalytic activity for NO reduction by CO.[10,11] It was also reported that with increasing reduction temperatures, the SSA ($m^2\ g^{-1}$) and surface density (# of atoms per nm^2) were decreased and increased, respectively, using the same Ni wt%, ~10 wt%, on NiO_x/CeO_2 samples. To study the molecular structure (*i.e.*, monolayer) and compare the catalytic activity with different catalysts, the surface density of surface species has been applied instead of using surface species wt%.[17–20] T. C. Peck *et al.* reported that bulk oxide surface species were not observed up to 3.87 Fe per nm^2 and 1.22 Co per nm^2 for the series of FeO_x/CeO_2 and CoO_x/CeO_2 catalysts, respectively.[18] The authors also observed that microcrystalline surface species on FeO_x/CeO_2 (5.4 Fe per nm^2) and CoO_x/CeO_2 (3.57 Co per nm^2) showed higher catalytic activity, while decreased areal activity was obtained at lower or beyond the surface densities. T. Kim *et al.* studied the structure–activity relationship for methanol dehydration reaction over the series of metal oxide (*i.e.*, TiO_2, Nb_2O_5, Al_2O_3, and ZrO_2) supported WO_x catalysts and reported that the monolayer coverage surface density (~4.5 W nm^{-2}) could be independent of the supports.[20] In the case of catalytic activity, however, it was dependent on the specific oxide supports due to the different cation electronegativity.

Several researchers have investigated the effect of oxidation states of metal on their catalytic activity. S. Vivek *et al.* synthesized bimetallic copper and nickel nanoparticles and investigated the effect of oxidation states of bimetallic Cu–Ni on the catalytic activity and electrochemical properties.[21] The authors reported that the increased oxidation states of nickel and copper can enhance the catalytic activity. Wu *et al.* designed partially oxidized Ni/CeO_2 catalysts for steam methane reforming (SMR) reaction.[22] Especially, the author calculated the oxidation state of Ni to improve the SMR reaction by density functional theory (DFT) calculations. Based on DFT calculations, the author found that the oxidation state of Ni could affect the activity and stability of Ni/CeO_2 catalysts for the SMR reaction, and the partially oxidized Ni_4O/CeO_2 catalyst showed higher activity and good stability, which were verified experimentally. S. D. Senanayake *et al.* studied the interaction between Ni atom and CeO_2(111) surfaces over Ni–CeO_2(111) catalysts for water–gas shift (WGS) and CO methanation reactions using X-ray and ultraviolet photoelectron spectroscopies.[23] The authors found that Ni species remain in the metallic state at 300 K, while the CeO_2 substrate was partially reduced with the formation of Ni^{2+} at 500–800 K under WGS and CO methanation reactions. It was claimed that the presence of metallic Ni species could promote a strong interaction between chemisorbed CO and the admetal at 300 K. J. Carrasco *et al.* also investigated the interaction between Ni species and CeO_2(111) surfaces to analyze the charge transfer, oxidation states, and perturbation in the Ni density-of-states by DFT calculations.[24] They also compared the adsorption of CO and C on the Ni_n (n = 1 and 4) particles because the formation of coke layers on the surface during the methanation reaction affects the catalytic performance. The authors found that methanation activity was closely related to the oxidation states of Ni, and Ni/CeO_2(111) was less likely to facilitate coke formation. Although several studies have reported oxidation state effects on catalytic activity, a direct comparison between oxidized and reduced catalysts for physicochemical properties and catalytic activity is still lacking.

In the current work, the NO reduction by CO over oxidized and reduced NiO_x supported on CeO_2 catalysts was investigated to understand the relationship between catalyst synthesis conditions and the physicochemical properties of the catalysts as well as catalytic performance. Since the Ni surface density should be affected by the support treatment conditions with the same Ni loading (*i.e.*, higher treatment temperature and higher Ni surface density), for comparison purposes, it was fixed as 5.3 Ni per nm^2. The physicochemical properties of the prepared catalysts were analyzed by the Brunauer–Emmett–Teller (BET) technique, inductively coupled plasma/optical emission spectroscopy (ICP/OES), Raman (Visible and UV), X-ray photoelectron spectroscopy (XPS), and synchrotron X-ray diffraction (S-XRD) spectroscopy. Furthermore, to evaluate the catalytic activity and understand the intermediate species during the NO reduction by CO, gas chromatography (GC) and diffuse reflectance infrared Fourier transform spectroscopy (DRIFTS) were applied.

2. Experimental section

2.1 Catalyst synthesis

For oxidized and reduced NiO_x/CeO_2 catalysts, the two-step synthesis method was applied. First, the as-received bulk CeO_2 (HAS 5, Rhodia) was pretreated (oxidizing and reducing) at different temperatures (400, 500, and 700 °C) for 6 h (oxidation, dry air, 20% oxygen and 80% nitrogen, total flow rate of 100 ml min^{-1}, Airgas) or 3 h (reduction, 5% H_2 balanced with N_2, total flow rate of 50 ml min^{-1}, Airgas) before being used as support materials for NiO_x/CeO_2 catalysts.

The supported nickel oxide (NiO_x) catalysts were synthesized with a fixed surface density of 5.3 Ni per nm^2 using the incipient wetness impregnation (IWI) method. Various concentrations of nickel(II) nitrate hexahydrate (98% $Ni(NO_3)_2\cdot 6H_2O$, Alfa Aesar) were dissolved in de-ionized water to make precursor solutions, and then the precursor solution was dropped onto the pretreated CeO_2 powder while mixing constantly. After impregnation, the mixture was dried at room temperature for 12 h. The dried sample was transported to a combustion boat and further dried at 120 °C under flowing air (dry air, 20% oxygen and 80% nitrogen, total flow rate of 100 ml min^{-1}, Airgas) inside a tube furnace (Lindberg/Blue Mini-Mite, Thermo) for 12 h. Finally, the catalysts were subsequently treated in the air (dry air, 20% oxygen and 80% nitrogen, total flow rate of 100 ml min^{-1}, Airgas) at different temperatures (400, 500, and 700 °C) for 6 h to complete the oxidation process and sieved (425 μm, Fieldmaster). The synthesized CeO_2-supported nickel oxide catalysts were denoted as 5.3 NiO_x/CeO_2-400Oxi, 5.3 NiO_x/CeO_2-500Oxi, and 5.3 NiO_x/CeO_2-700Oxi. The reduced samples were also dried using the same method as described above and the catalysts with a fixed surface density (5.3 Ni per nm^2) were first pretreated under N_2 (UHP, 100 ml min^{-1}, Airgas) atmosphere at 400 °C for 30 min and then reduced in H_2 flow (5 vol% H_2 balanced with N_2, total flow rate of 50 ml min^{-1}, Airgas) at different temperatures (400, 500, and 700 °C) for 3 h. The reduced catalysts were denoted as 5.3 NiO_x/CeO_2-400R, 5.3 NiO_x/CeO_2-500R, and 5.3 NiO_x/CeO_2-700R.

2.2 Catalyst characterization

The specific surface area (SSA) and average pore volume of catalysts were calculated from nitrogen adsorption and desorption isotherms (Micromeritics ASAP 1010) using multipoint BET and BJH methods, respectively. Prior to analysis, the catalysts were degassed at 300 °C for 4 h under a vacuum to remove the moisture, impurities, and volatiles. To determine the Ni content in the NiO_x/CeO_2 catalysts, the concentration of Ni was analyzed using ICP/OES (Optima 5300DV, PerkinElmer). Prior to the ICP/OES analysis, the catalysts were pretreated with 0.01 g of catalyst and 10 mL of nitric acid (70% HNO_3) using a microwave digestion system (ETHOS TC, Milestone). Molecular structures and bonding vibrations of supported NiO_x catalysts were obtained *via* Raman spectroscopy. Raman spectra were collected with visible (532 nm, Horiba Raman spectrometer) laser (laser power = 100 mW) and UV (325 nm, Renishaw inVia Raman microscope) laser (laser power = 25 mW) under ambient conditions. The visible Raman spectra were collected in the 200–1400 cm^{-1} Raman shift regions and UV Raman spectra were collected in the range of 350–1500 cm^{-1}. For both visible and UV Raman spectra, the acquisition time was 10 seconds, and the final spectrum was accumulated from 60 scans. XPS analysis was performed to investigate the surface elemental compositions and chemical states of prepared samples using K-alpha (Thermo Scientific, USA). XPS data were obtained using monochromatic Al-Kα radiation ($h\nu$ = 1486.6 eV). To obtain high energy X-ray diffraction patterns, powder samples were loaded in polyimide (1 mm OD Kapton) tubes sealed with clay. The diffraction patterns were obtained at 28-ID-1 PDF beamline (74.53 keV, λ = 0.16635 Å) at National Synchrotron Light Source II (NSLS-II) at Brookhaven National Laboratory (BNL). Dioptas was used to obtain one-dimensional (1D) data from the two-dimensional (2D) scattering pattern.

2.3 Catalyst activity test

The gas phase reactions were performed in a fixed bed quartz reactor (OD 9.6 mm, ID 7 mm) packed with sieved catalyst powder (40 mg) at 25–500 °C under atmospheric pressure. For the experiment, the catalyst was loaded into the quartz reactor and held in place by a quartz wool. Flow rates were measured by mass flow controllers (SLA5800 Series, Brooks Instrument), and the temperature was monitored by a K-type thermocouple (Omega). Reaction products were identified and analyzed by TRACE™ 1300 GC (Thermo Scientific) containing a capillary column (Carboxen® 1010 PLOT) equipped with the thermal conductivity detector (TCD). Before the activity test, the prepared catalysts were pretreated at 400 °C in He (30 mL min^{-1}) for 30 min with a ramping rate of 10 °C min^{-1}. For the NO reduction by CO, the gas mixtures were 5% NO (20 ml min^{-1} of 10% NO with He balance, Airgas) and 5% CO (20 ml min^{-1} of 10% CO with He balance, General Welding). The total flow rate was 40 mL min^{-1} in all experiments, and the reaction temperature was increased up to 500 °C with a ramping rate of 1 °C min^{-1}.

2.4 *In situ* diffuse reflectance infrared Fourier transform spectroscopy (*in situ* DRIFTS)

The *in situ* DRIFTS experiments were performed with a Thermo Scientific Nicolet iS10 FT-IR (4 cm^{-1} spectral resolution, 32 average scans) and a Harrick Praying Mantis chamber. The catalyst sample was first pretreated at 400 °C in flowing He (UHP, 30 ml min^{-1}) for 30 min. After pretreatment, the sample was cooled to room temperature under flowing He, and a background spectrum was taken. The DRIFTS spectra were collected at different reaction temperatures, room temperature to 500 °C, with the gas mixtures of 5% NO (20 ml min^{-1} of 10% NO with He balance) and 5% CO (20 ml min^{-1} of 10% CO with He balance). To further study the formation of intermediate species in addition to the gas phase products, the DRIFTS spectra with increasing exposure time (2–30 min) at 170 °C were also collected under the following conditions: (1) CO pre-adsorption and NO reaction with CO pretreated samples, (2)

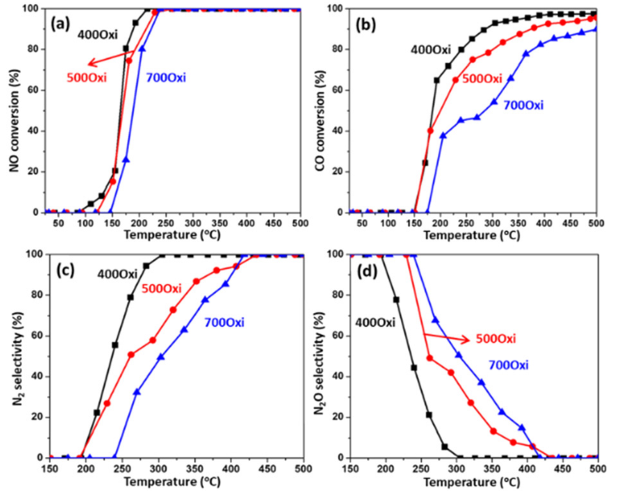

Fig. 1 The catalytic activity of oxidized 5.3 NiO_x/CeO_2 catalysts for the NO reduction by CO at different reaction temperatures. (a) The NO conversion, (b) CO conversion, (c) N_2 selectivity, and (d) N_2O selectivity. Reaction conditions: 5% NO and 5% CO balanced with helium, total flow rate = 40 ml min^{-1}, and GHSV = 60 000 ml g^{-1} h^{-1}.

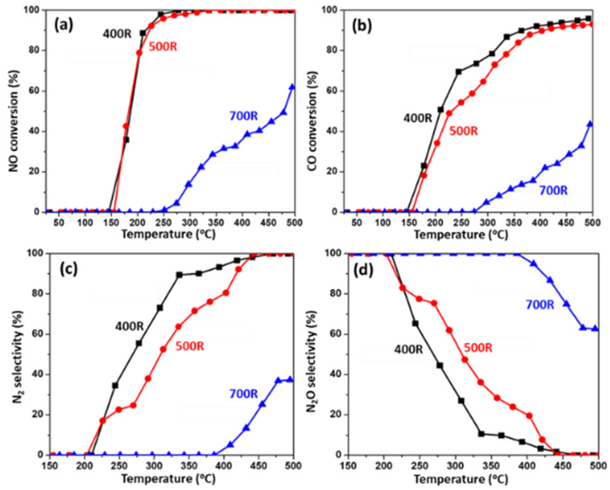

Fig. 2 The catalytic activity of reduced 5.3 NiO_x/CeO_2 catalysts for the NO reduction by CO at different reaction temperatures. (a) The NO conversion, (b) CO conversion, (c) N_2 selectivity, and (d) N_2O selectivity. Reaction conditions: 5% NO and 5% CO balanced with helium, total flow rate = 40 ml min^{-1}, and GHSV = 60 000 ml g^{-1} h^{-1}.

NO pre-adsorption and CO reaction with NO pretreated samples, and (3) NO and CO co-adsorption.

3. Results

3.1 Catalytic activity test of NO reduction by CO

Fig. 1 and 2 show the catalytic activity results of the oxidized and reduced 5.3 NiO_x/CeO_2 catalysts for the NO reduction by CO as a function of reaction temperature. For all samples, both NO and CO conversions were increased with increasing reaction temperatures. In the case of oxidized 5.3 NiO_x/CeO_2 catalysts, the NO conversion was slightly decreased with increasing synthesis temperatures, while CO conversions were significantly affected by the synthesis temperatures, as shown in Fig. 1(a) and (b). It was also noticed that NO conversion was higher than CO conversion under the experimental conditions. As shown in Fig. 2(a) and (b), reduced samples showed similar trends (higher reduction temperatures and lower NO and CO conversions) with oxidized samples. Similar to the oxidized samples, the reduced samples also showed a higher NO conversion than CO conversion at >150 °C. Among the tested oxidized and reduced samples, 5.3 NiO_x/CeO_2-700R showed the lowest catalytic activity (62% for NO conversion and 44% for CO conversion at 500 °C). Overall, the oxidized and reduced NiO_x/CeO_2 catalysts showed decreased catalytic activities with increasing treatment temperature, and the effect of pretreatment on the NO reduction by CO reaction over supported NiO_x catalysts shows the following trend: (1) NO conversion: 400Oxi ≈ 500Oxi > 400R ≈ 500R ≈ 700Oxi ≫ 700R. (2) CO conversion: 400Oxi > 500Oxi > 400R > 500R > 700Oxi ≫ 700R. It should be noted that the treatment temperature had a greater effect on the CO conversion than the NO conversion, even at mild oxidation and reduction temperatures, such as 400 °C and 500 °C. The N_2 and N_2O selectivities were also evaluated, and the results are shown in Fig. 1(c)–(d) and 2(c)–(d). As shown in the selectivity results, N_2O was produced at a lower temperature, while N_2 selectivity was increased with increasing reaction temperatures. The detailed reaction mechanism of intermediate N_2O species will be further discussed in the DRIFTS section.

3.2 Physical properties of the catalysts

To understand the relationship between physical properties and catalytic activity of the prepared catalysts, the BET specific surface area (SSA), total pore volume, and average pore diameter were investigated by the nitrogen adsorption and desorption isotherms. The isotherm curves of 400 °C and 500 °C pretreated samples (oxidized and reduced) exhibited type IV isotherms with a H1-type hysteresis loop (Fig. 3(a) and (b)), implying that catalysts consist of mesoporous structures.[25,26] The 700 °C pretreated samples (700Oxi and 700R), however, showed type V isotherms with a H3 hysteresis loop, indicating pores and a relatively large pore size. (Fig. 3(a) and (b)) Compared to the bulk CeO_2 that contains a mesopore structure as reported in our previous research,[11] the oxidized and reduced NiO_x/CeO_2 catalysts at 400 °C and 500 °C showed similar isotherm curves, indicating that the mesoporous structure of CeO_2 was maintained even after introducing NiO_x (5.3 Ni per nm^2) and thermal treatment. The specific surface area (SSA), Ni wt%, surface density (SD) from NiO_x/CeO_2 sample's SSA, total pore volume, and average pore diameter are listed in Table 1. It is noted that to fix the surface density (5.3 Ni atoms per nm^2, as a target SD) of supported NiO_x catalysts, Ni wt% was calculated based on the SSA of pretreated CeO_2 supports. As shown in Table 1, experimentally obtained SD values, 5.6–6.8 Ni per nm^2, were similar to or higher than that of the target value, 5.3 Ni per nm^2. The Ni wt% and SD values of oxidized and reduced samples were also measured by ICP-OES, and the results are included in Table 1. Compared to the bulk CeO_2 (as-received), the SSA of pretreated NiO_x/CeO_2 decreased with increasing pretreatment temperature, while the pore diameter increased due to sintering of CeO_2 under high treatment temperatures, especially at 700 °C.

3.3 Raman spectroscopy

For investigating the detailed molecular structure of oxidized and reduced 5.3 NiO_x/CeO_2 catalysts, Raman spectroscopy

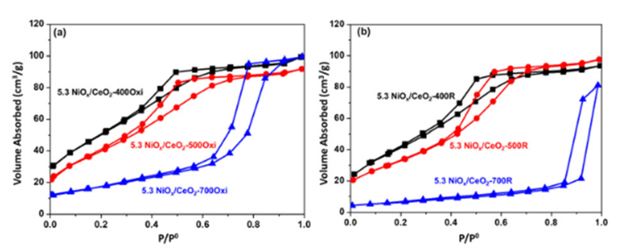

Fig. 3 The N_2 adsorption–desorption isotherms of the (a) oxidized and (b) reduced 5.3 NiO_x/CeO_2 catalysts.

Table 1 The specific surface area, surface density, total pore volume, and average pore size of the NiO_x/CeO_2 catalysts

Sample[a]	SSA (m^2 g^{-1})	Ni wt (%)	SD[b] (Ni per nm^2)	Ni wt[c] (%)	SD[d] (Ni per nm^2)	Total pore volume (cm^3 g^{-1})	Average pore diameter (nm)
Bulk CeO_2[e]	216	—	—	—	—	0.16	1.5
5.3 NiO_x/CeO_2-400Oxi	180	9.9	5.6	9.42	5.37	0.15	1.7
5.3 NiO_x/CeO_2-500Oxi	150	9.4	6.4	8.46	5.78	0.14	1.9
5.3 NiO_x/CeO_2-700Oxi	59	3.9	6.8	3.35	5.83	0.15	5.2
5.3 NiO_x/CeO_2-400R	158	9.8	6.4	8.45	5.49	0.14	1.8
5.3 NiO_x/CeO_2-500R	129	8.2	5.7	7.62	6.06	0.15	2.3
5.3 NiO_x/CeO_2-700R	22	1.4	6.5	1.35	6.29	0.12	11.4

[a] 5.3 is the surface density of Ni (Ni per nm^2) using support's SSA $= \frac{\frac{W_{Ni}}{100}\times 6.02\times 10^{23}\times \frac{1}{M_{Ni}}}{S\times\left(1-\frac{W_{Ni}}{100}\right)\times 10^{18}}$ where W_{Ni} is the weight percentage of Ni, M_{Ni} is the atomic weight of Ni (58.7 g mol^{-1}), and S is the SSA of the oxidized or reduced CeO_2 sample. [b] Surface density of Ni (Ni per nm^2) using sample's SSA $= \frac{\frac{W_{Ni}}{100}\times 6.02\times 10^{23}\times \frac{1}{M_{Ni}}}{S\times 10^{18}}$ where W_{Ni} is the weight percentage of Ni, M_{Ni} is the atomic weight of Ni (58.7 g mol^{-1}), and S is the SSA of the oxidized or reduced 5.3 NiO_x/CeO_2 sample. [c] Ni weight percent obtained by ICP/OES. [d] Surface density of Ni (Ni per nm^2) using sample's SSA $= \frac{\frac{W_{Ni}}{100}\times 6.02\times 10^{23}\times \frac{1}{M_{Ni}}}{S\times 10^{18}}$, where the W_{Ni} was obtained by ICP/OES. [e] Results from ref. 11.

was performed. As shown in Fig. 4(I) and (II), the visible Raman spectra showed a dominant peak at ~460 cm^{-1}, which corresponded to the intrinsic F_{2g} symmetric vibrational mode of fluorite CeO_2, with weak bands at ~236 cm^{-1} and ~600 cm^{-1} due to the second-order transverse acoustic (2TA) mode and oxygen vacancy/defect induced (D) mode, respectively.[27–30] Based on our previous work,[11] the broad peak at 540 cm^{-1} could be assigned to a related NiO_x band. For both oxidized and reduced catalysts, the F_{2g} peak (~460 cm^{-1}) became narrower and sharper (a decreased full width at half maximum (FWHM)) with increasing pretreatment temperature due to increased crystallinity. The peak position of F_{2g} was slightly shifted (461 to 468 cm^{-1} (Oxi) and 469 cm^{-1} (Red)) with increasing pretreatment temperature, and the peak positions of the D band (~600 cm^{-1}) for both oxidized and reduced samples were not shifted. Based on visible Raman spectra results of oxidized and reduced catalysts, the concentration of oxygen vacancies (N) can be calculated using the spatial correlation model from the relationship between the grain size (d_g) and correlation length (average distance between two lattice defects, L). The detailed equations are provided as follows:

$$\Gamma = \frac{51.8}{d_g} + 5 \text{ or } d_g = \frac{51.8}{(\Gamma - 5)} \quad (1)$$

$$L(\text{nm}) = \sqrt[3]{\left(\frac{\alpha}{2d_g}\right)^2\left[\left(d_g - 2\alpha\right)^3 + 4d_g^2\alpha\right]} \quad (2)$$

$$N = \frac{3}{4\pi L^3} \quad (3)$$

where Γ is the HWHM of the F_{2g} peak (~460 cm^{-1}) of CeO_2, d_g is the grain size of CeO_2, L is the correlation length of CeO_2, and α is the radius (0.34 nm) of CeO_2 units.[28,30] As shown in Table 2, the grain size of CeO_2 (d_g) and correlation length (L) were increased with increasing temperatures, while the concentrations of oxygen vacancies (N) were decreased with increasing temperatures. The observed results show a similar trend to the SSA values shown in Table 1.

It was reported that UV Raman spectra can provide more detailed information on defect sites of CeO_2 due to the resonance Raman effect resulting from the strong absorption of CeO_2 in the UV region.[31–33] To better understand the oxygen vacancies (or defect sites) of CeO_2-supported NiO_x catalysts, UV Raman spectra were collected. Fig. 5 displays the UV Raman spectra of oxidized and reduced 5.3 NiO_x/CeO_2 catalysts. Compared to visible Raman spectra, UV Raman spectra showed a new peak at ~1180 cm^{-1}, which could be ascribed to the second-order longitudinal (2LO) mode.[29,30] It is worth noting that the peak intensity of the 2LO band (~1180 cm^{-1}) is as strong as the F_{2g} band (~460 cm^{-1}) due to the enhancement of the longitudinal (LO) overtones under the UV region.[34] Furthermore, the peak position of the 2LO band was shifted from 1140 cm^{-1} to 1180 cm^{-1} as the oxidation temperature increased, indicating that the Ce–O bond became stronger with increasing oxidation temperature.[3] In the case of the reduced samples, however, the 2LO bands were not much affected by the reduction temperatures (Fig. 5(II)). As shown in the insets of Fig. 5, the

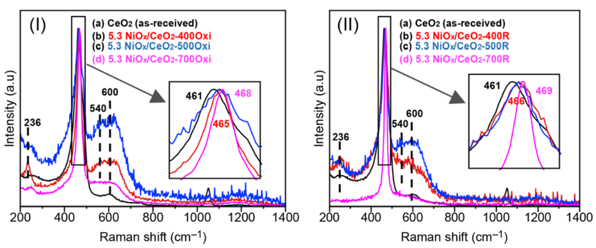

Fig. 4 The visible Raman spectra of (I) oxidized 5.3 NiO_x/CeO_2 ((a) CeO_2, (b) 5.3 NiO_x/CeO_2-400Oxi, (c) 5.3 NiO_x/CeO_2-500Oxi, and (d) 5.3 NiO_x/CeO_2-700Oxi), (II) reduced 5.3 NiO_x/CeO_2 ((a) CeO_2, (b) 5.3 NiO_x/CeO_2-400R, (c) 5.3 NiO_x/CeO_2-500R, and (d) 5.3 NiO_x/CeO_2-700R).

Table 2 The grain size (d_g), correlation length (L), concentration of oxygen vacancies (N), and defect ratio ($I_D/I_{F_{2g}}$) of the oxidized and reduced 5.3 NiO_x/CeO_2 catalysts

Catalyst	Grain size of CeO_2 (d_g, nm)	Correlating length (L, nm)	Concentration of oxygen vacancies ($N \times 10^{-21}$, cm^{-3})	Defect ratio ($I_D/I_{F_{2g}}$)
Bulk CeO_2	2.77	0.42	3.24	1.06[a]
5.3 NiO_x/CeO_2-400Oxi	3.07	0.43	2.93	0.91
5.3 NiO_x/CeO_2-500Oxi	3.96	0.47	2.28	0.74
5.3 NiO_x/CeO_2-700Oxi	7.63	0.59	1.15	0.40
5.3 NiO_x/CeO_2-400R	3.63	0.46	2.49	0.56
5.3 NiO_x/CeO_2-500R	4.34	0.49	2.08	0.33
5.3 NiO_x/CeO_2-700R	17.25	0.78	0.49	0.18

[a] Results from ref. 35.

relative intensity ratio of the defect vibration ($I_D/I_{F_{2g}}$) for both oxidized and reduced catalysts decreased with increasing pretreatment temperatures, suggesting that the thermal effect induced a decrease in oxygen vacancy/defect sites. For the concentration of oxygen vacancies (N) and defect ratio ($I_D/I_{F_{2g}}$), as shown in Table 2, the values for both oxidized and reduced catalysts decreased with increasing treatment temperatures. Although the trends of the defect ratio were similar, the reduced catalysts showed a lower defect concentration than those of the oxidized samples, indicating that both treatment temperature and gas compositions affected oxygen vacancies and defect sites.

3.4 X-ray photoelectron spectroscopy (XPS)

XPS analysis was performed to illuminate oxidation states and surface composition of prepared catalysts. Fig. 6(a) shows the deconvoluted core level Ce 3d XPS spectra in the 925–875 eV range for 5.3 NiO_x/CeO_2 catalysts oxidized at 400, 500, and 700 °C. In this range, the Ce 3d spectra consist of the u band ($3d_{3/2}$) and v band ($3d_{5/2}$), which are further resolved into ten sub-peaks (u_0, u, u', u'', u''', v_0, v, v', v'', and v''').[35,36] The four sub-peaks, v_0 (~880.11 eV), v' (~882.54 eV), u_0 (~899.20 eV), and u' (~903.51 eV), correspond to Ce^{3+} species, while the remaining six sub-peaks, v (~882.47 eV), v'' (~888.87 eV), v''' (~898.27 eV), u (~903.51 eV), u'' (~907.47 eV), and u''' (~916.74 eV), are related to Ce^{4+} species, and peak shifts between samples were rarely observed. These are highlighted in Fig. 6(a) and (b), with the sub-peaks corresponding to Ce^{3+} shown in red and sub-peaks corresponding to Ce^{4+} in blue. Calculating the area ratios of these sub-peaks allows us to assess the relative content of Ce^{3+} on the surface of the catalysts. Table 3 provides the values obtained by dividing the Ce^{3+} area by the sum of Ce^{3+} and Ce^{4+} areas. The Ce^{3+} ratio in 5.3 NiO_x/CeO_2-400Oxi (24%) and 5.3 NiO_x/CeO_2-500Oxi (24%) samples were similar. However, in the case of 5.3 NiO_x/CeO_2-700Oxi, the Ce^{3+} ratio decreased to 18%. The reduced catalysts were also subjected to peak deconvolution in the same manner (Fig. 6(b)), and the Ce^{3+} ratio was determined (Table 3). In the reduced catalysts, the Ce^{3+} ratio continuously decreased with increasing reduction temperatures.

In the case of Ni $2p_{3/2}$, three distinct sub-peaks, located at 853.5, 855.8, and 861.5 eV, were observed, which are attributed to Ni^{2+} in NiO, Ni^{3+}, and satellite peaks, respectively (Fig. 6(c) and (d)).[37,38] It is noted that only the Ni $2p_{3/2}$ region was analyzed because of the overlap between the Ce 3d peak and the Ni $2p_{1/2}$ peak. The samples subjected to oxidation show a slight increase in the peak intensity at the approximately 855.8 eV peak assigned to Ni^{3+} compared to the 853.5 eV peak assigned to Ni^{2+} at both 400 and 500 °C. The catalyst oxidized at 700 °C exhibits a low Ni content, making it challenging to achieve high intensity, but it appears to have a high Ni^{3+} content compared to Ni^{2+}. To quantitatively assess the change in the oxidation state of Ni with temperature, the area of Ni^{3+} was divided by the sum of Ni^{2+} and Ni^{3+} areas (Table 3). For the oxidized catalysts, there was no substantial difference between 400 and 500 °C, with values of 0.68 and 0.70, respectively. In the case of the reduced catalysts, it is evident that the peak intensity at 855.8 eV increases significantly even with the temperature difference between 400 and 500 °C (Fig. 6(d)). When calculating the relative area ratio of Ni^{3+} in the same manner as the oxidized samples, the value is 0.71 at 400 °C, and when treated at 500 °C, it increases to 0.83. This indicates that the oxidation state of Ni is sensitive to changes under reducing conditions. Similar to the XPS data of the 700Oxi sample, the 700R sample also exhibited low Ni peaks. Although quantifying the Ni^{3+} ratio was difficult, the intensity of the Ni^{3+} peak was relatively higher than that of Ni^{2+}.

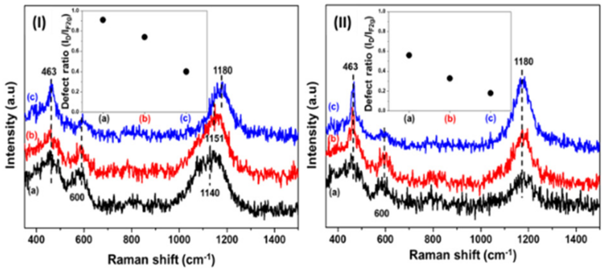

Fig. 5 The UV-Raman spectra of (I) oxidized 5.3 NiO_x/CeO_2 ((a) 5.3 NiO_x/CeO_2-400Oxi, (b) 5.3 NiO_x/CeO_2-500Oxi, and (c) 5.3 NiO_x/CeO_2-700Oxi), (II) reduced 5.3 NiO_x/CeO_2 ((a) 5.3 NiO_x/CeO_2-400R, (b) 5.3 NiO_x/CeO_2-500R, and (c) 5.3 NiO_x/CeO_2-700R); inset: the defect ratio of oxidized and reduced catalysts. Defect ratio = I_D (600 cm^{-1})/$I_{F_{2g}}$ (464 cm^{-1}).

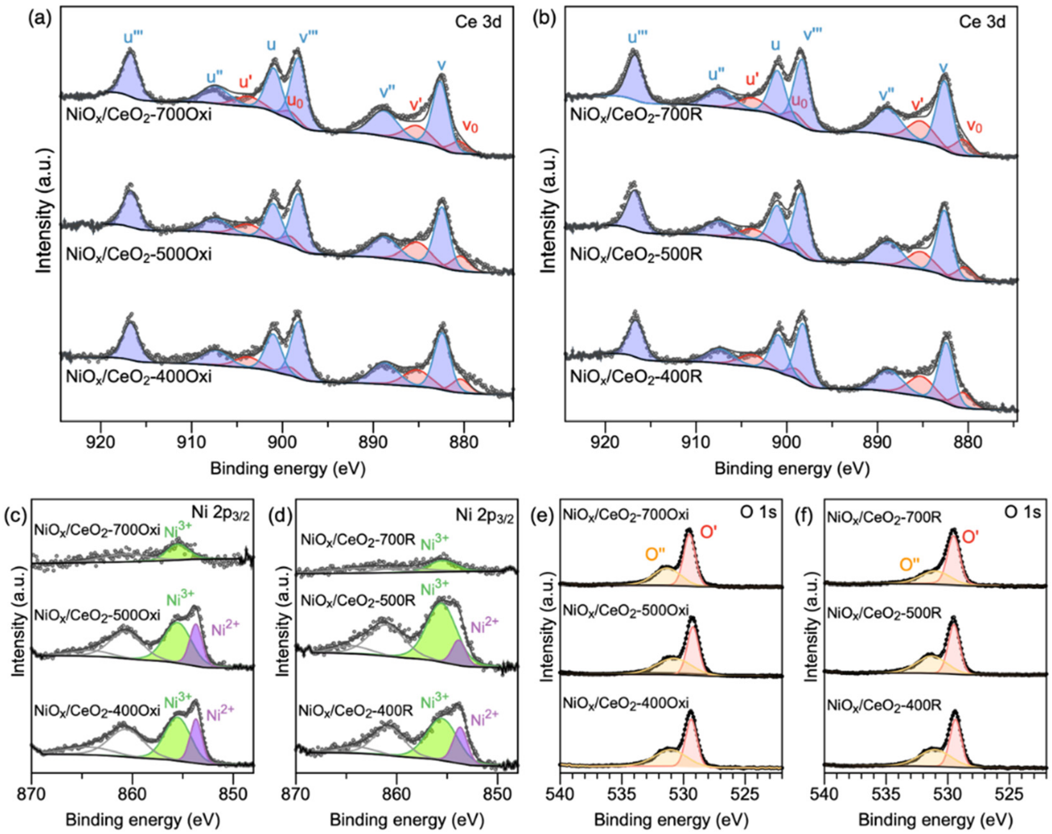

Fig. 6 The deconvoluted Ce 3d XPS spectra of (a) oxidized 5.3 NiO_x/CeO_2 and (b) reduced 5.3 NiO_x/CeO_2. The deconvoluted Ni $2p_{3/2}$ XPS spectra of (c) oxidized 5.3 NiO_x/CeO_2 and (d) reduced 5.3 NiO_x/CeO_2. The deconvoluted O 1s XPS spectra of (e) oxidized 5.3 NiO_x/CeO_2 and (f) reduced 5.3 NiO_x/CeO_2.

Table 3 The ratio of Ce^{3+} compared to Ce^{3+} + Ce^{4+}, the ratio of Ni^{3+} compared to Ni^{2+} + Ni^{3+}, and the ratio of O″ compared to O′ on the surface of oxidized 5.3 NiO_x/CeO_2 and reduced 5.3 NiO_x/CeO_2

Sample	$Ce^{3+}/(Ce^{3+} + Ce^{4+})$ (mol mol^{-1})	$Ni^{3+}/(Ni^{2+} + Ni^{3+})$ (mol mol^{-1})	O″/O′ (mol mol^{-1})
5.3 NiO_x/CeO_2-400Oxi	0.24	0.68	1.01
5.3 NiO_x/CeO_2-500Oxi	0.24	0.70	1.01
5.3 NiO_x/CeO_2-700Oxi	0.18	—	0.84
5.3 NiO_x/CeO_2-400R	0.27	0.71	1.00
5.3 NiO_x/CeO_2-500R	0.21	0.83	0.90
5.3 NiO_x/CeO_2-700R	0.19	—	0.64

Fig. 6(e) and (f) show the deconvoluted O 1s XPS spectra in the 540–520 eV range for all samples. The O 1s peak could be deconvoluted into two sub-peaks. The peak at 529.21 eV (O′) corresponds to lattice oxygen, while the peak at 530.83 eV (O″) corresponds to oxygen present in absorbed species such as carbonates and hydroxyl groups.[37,38] By calculating the area ratio of these two peaks, the concentration of oxygen vacancies on the catalyst surface could be obtained indirectly. In the case of oxidized catalysts, the O″/O′ ratio of 5.3 NiO_x/CeO_2-400Oxi and 5.3 NiO_x/CeO_2-500Oxi both exhibit values of 1.01, showing no difference. At 700 °C, the ratio of O″ significantly decreased to 0.84. This trend aligns with the $Ce^{3+}/(Ce^{3+}+Ce^{4+})$ ratio. For the reduced catalysts, the ratio was 1.00 for 5.3 NiO_x/CeO_2-400R, but as the heat treatment temperature increased to 500 °C (5.3 NiO_x/CeO_2-500R), it dropped to 0.90, indicating that the heat treatment temperature under reducing conditions affected the oxidation states of catalysts. Furthermore, at 700 °C, the O″ ratio decreased significantly to 0.64.

3.5 Powder X-ray diffraction (XRD)

To understand the effect of oxidation and reduction treatments on the crystalline structure of NiO_x/CeO_2 catalysts, synchrotron-based X-ray diffraction (s-XRD) spectra were collected (Fig. 7). For all the supported NiO_x catalysts, the fluorite CeO_2 (□ symbol) peaks (JCPDS-ICDD Card No. 34-394) at 3.0° (111), 3.5° (200), 4.9° (220), 5.8° (311), 6.1° (222),

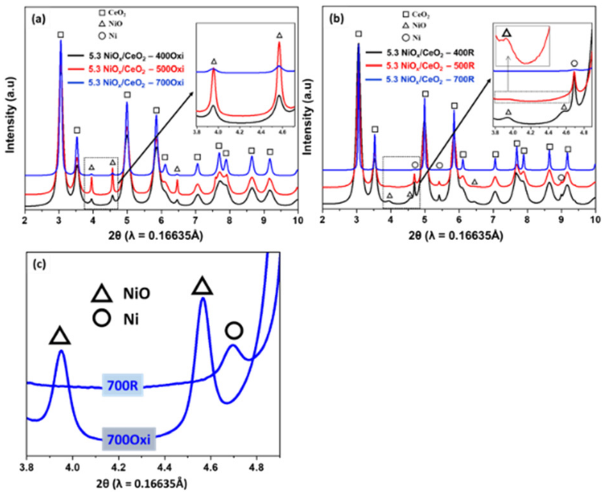

Fig. 7 The XRD patterns of (a) oxidized 5.3 NiO_x/CeO_2, (b) reduced 5.3 NiO_x/CeO_2 catalysts, and (c) 700Oxi and 700R 5.3 NiO_x/CeO_2.

7.0° (400), 7.6° (331), 7.8° (420), 8.6° (422), and 9.1° (511) were clearly observed, especially for the 700 °C-treated samples. In addition to the fluorite CeO_2 peaks, oxidized 5.3 NiO_x/CeO_2 catalyst contained nickel oxide (△ symbol) peaks at 3.9°, 4.5°, and 6.4°, which can be ascribed to the (111), (200), and (220) reflections of nickel oxide, respectively (JCPDS-ICDD Card No.04-0835).

As shown in the inset Fig. 7(a), the intensity of nickel oxide peaks increased with increasing temperature up to 500 °C, while the peak intensity drastically decreased at 700 °C due to the relatively lower Ni concentration (3.9 wt%) of the 5.3 NiO_x/CeO_2-700Oxi sample. For the reduced 5.3 NiO_x/CeO_2 catalysts, there were new peaks (○ symbol) at 4.7°, 5.4°, 8.9°, and 9.3°, which can be ascribed to the (111), (200), (311), and (222) reflections of fcc Ni (JCPDS-ICDD Card No. 04-0850 (fcc)), respectively (Fig. 7(b) and (c)). For 5.3 NiO_x/CeO_2-400R and 500R samples, nickel oxide peaks were still retained, indicating that the nickel species were not fully reduced at 400 and 500 °C, while the 700R samples contained only metallic nickel species (Fig. 7(c)). Note that the Ni peak intensity was very low in the 700R sample's XRD pattern due to the low Ni concentration (1.4 wt%). For both oxidized and reduced catalysts, the CeO_2 (111) peak became sharper with increasing treatment temperatures, suggesting that the crystallite size of CeO_2 was changed as the pretreatment temperature increased. The CeO_2 crystallite sizes of prepared samples were calculated using the Scherrer's equation and are listed in Table 4. For both oxidized and reduced samples at 700 °C, the average CeO_2 crystallite size was drastically increased, while the lattice parameter of CeO_2 was not changed, suggesting that sintering at high temperature induced the larger crystallites and increased the crystallinity of the pretreated samples. Compared to the 5.3 NiO_x/CeO_2-700Oxi catalyst (11.13 nm), the reduced catalyst at 700 °C showed a larger crystallite size (20.96 nm), indicating that not only the treatment temperature but also the reducing condition could have an enhanced sintering effect.

3.6 Diffuse reflectance infrared Fourier transform spectroscopy (DRIFTS)

When comparing the catalytic activities of oxidized and reduced catalysts, it was observed that the catalyst activity decreases as the pretreatment temperature increases (Fig. 1 and 2). Furthermore, even at the same treatment temperature, the catalyst activity was lower when treated in the reducing condition compared to the oxidizing condition. In conclusion, the catalyst exhibited the highest activity when pretreated at a relatively low temperature of 400 °C in the oxidizing condition, while the catalyst activity was lowest when pretreated at a relatively high temperature of 700 °C in the reducing condition. To investigate the interaction between the reactants (NO and CO) and catalyst surface as well as the formation of the intermediate species, *in situ* DRIFTS analysis was performed for 5.3 NiO_x/CeO_2-400Oxi (highest activity) and 5.3 NiO_x/CeO_2-700R (lowest activity) catalysts in the temperature range of 50–500 °C. As shown in Fig. 8(a), *in situ* DRIFTS spectra of the oxidized 5.3 NiO_x/CeO_2 sample exhibited absorbance peaks corresponding to various NO and CO-based intermediate surface species.

For the NO-based surface species, the following peaks were observed from 50 °C to 220 °C: bridging bidentate nitrate at 1010 cm^{-1}, bidentate nitrate (or linear nitrite or monodentate nitrate) in the range of 1227–1308 cm^{-1} and monodentate nitrate (or bridging nitro or bridging bidentate nitrate) in the range of 1535–1608 cm^{-1}.[39,40] Additionally, a minor peak at 1241 cm^{-1} was observed, corresponding to

Table 4 The CeO_2 (111) peak position, full width half maximum (FWHM), calculated crystallite size, and lattice parameters of the oxidized and reduced 5.3 NiO_x/CeO_2 catalysts

Sample	CeO_2 (111) peak position (°)	CeO_2 (111) FWHM (°)	Crystallite size[a] (nm)	Lattice parameter[b] (Å)
5.3 NiO_x/CeO_2-400Oxi	3.05	0.16	5.41	5.41
5.3 NiO_x/CeO_2-500Oxi	3.05	0.14	6.00	5.41
5.3 NiO_x/CeO_2-700Oxi	3.05	0.08	11.13	5.41
5.3 NiO_x/CeO_2-400R	3.05	0.15	5.78	5.41
5.3 NiO_x/CeO_2-500R	3.05	0.12	7.12	5.41
5.3 NiO_x/CeO_2-700R	3.05	0.04	20.96	5.41

[a] $D = 0.9\lambda/(\beta \cdot \cos\theta)$. [b] $a = \sqrt{h^2 + k^2 + l^2} \cdot d_{111} = \sqrt{3} d_{111}$, $d_{111} = \dfrac{\lambda}{2 \cdot \sin\theta_{111}}$ where D is the crystallite size, λ is the X-ray wavelength (0.16635 Å), β is the FWHM of the CeO_2 (111) peak, θ is the Bragg angle of the peak, a is the lattice parameter, and d is the spacing of (111) lattice planes.

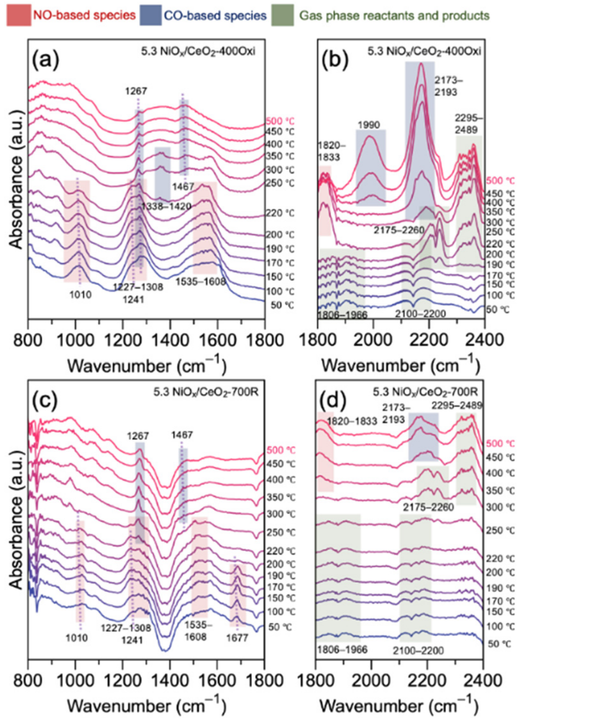

Fig. 8 The *in situ* DRIFTS of (a) 5.3 NiO_x/CeO_2-400Oxi (800–1800 cm^{-1}), (b) 5.3 NiO_x/CeO_2-400Oxi (1800–2400 cm^{-1}), (c) 5.3 NiO_x/CeO_2-700R (800–1800 cm^{-1}), and (d) 5.3 NiO_x/CeO_2-700R (1800–2400 cm^{-1}) in NO reduction by CO at different temperatures. Reaction conditions: 5% NO, 5% CO balanced with helium, and temperature = 50–500 °C.

monodentate nitrate.[41,42] For the CO-based surface species, the following peaks were observed: bidentate carbonate at 1267 cm^{-1} (≥150 °C), monodentate carbonate or carboxylate in the range of 1338–1420 cm^{-1} and bidentate carbonate at 1467 cm^{-1} (≥220 °C).[43–45] The 5.3 NiO_x/CeO_2-700R sample displayed slightly different DRIFTS spectra compared to the 5.3 NiO_x/CeO_2-400Oxi sample (Fig. 8(c)): (I) NO-based intermediate species' peak intensity was relatively weak, (II) monodentate carbonate or carboxylate peak (1338–1420 cm^{-1}) was not observed, while bidentate carbonate peak appeared at 200–250 °C, which was higher than that of 5.3 NiO_x/CeO_2-400Oxi (150–170 °C).

The generation of the intermediate surface species leads to several gaseous products (Fig. 8(b) and (d)). The weak band at 1806–1966 cm^{-1} was attributed to gas phase NO, and it disappeared at ≥200 °C (5.3 NiO_x/CeO_2-400Oxi) and ≥300 °C (5.3 NiO_x/CeO_2-700R), respectively. The gas phase CO (2100–2200 cm^{-1}) appeared at 50 °C and disappeared at >250 °C (5.3 NiO_x/CeO_2-400Oxi) and >350 °C (5.3 NiO_x/CeO_2-700R), respectively. The gas phase CO_2 peak at 2295–2489 cm^{-1} appeared at 200 °C (5.3 NiO_x/CeO_2-400Oxi), while those of 5.3 NiO_x/CeO_2-700R appeared at 300 °C, and their intensities increased as the reaction temperature increased. The N_2O intermediate surface species were also observed at 2175–2260 cm^{-1} and appeared at 170 °C (5.3 NiO_x/CeO_2-400Oxi) and 250 °C (5.3 NiO_x/CeO_2-700R), respectively.[8] In addition, NO and CO adsorption on the nickel oxide surface was also observed: 1820–1833 cm^{-1} (Ni^{+}/Ni^{2+}–NO or CO), 1990 cm^{-1} (Ni^{+}–CO), and 2173–2193 cm^{-1} (Ni^{2+}–CO), respectively.[47] It should be noted that the 5.3 NiO_x/CeO_2-700R sample contained only Ni based on the S-XRD results, as shown in Fig. 8(b) and (c). Although peak intensities of Ni^{+}/Ni^{2+}–NO and Ni^{2+}–CO are very weak, the *in situ* DRIFT result indicated that Ni on the 5.3 NiO_x/CeO_2-700R sample was partially oxidized during the reaction, especially at >300 °C. For the 5.3 NiO_x/CeO_2-700R sample, the Ni^{+}–CO peak (1990 cm^{-1}) was not observed, indicating that the CO adsorption on the surface was limited due to lower nickel concentration and surface area. As shown in Fig. 8, the NO adsorption peak appeared at lower temperatures than the CO adsorption peak. From these results, it can be hypothesized that the NO-based surface species could be adsorbed on the active sites (Ni^{+} or Ni^{2+}) at lower temperatures (<250 °C), and then the activated CO adsorption on the surface result in the replacement NO species at higher temperatures (Table 5).

4. Discussion

4.1 Pretreatment effect on the physicochemical properties of NiO_x/CeO_2 catalysts

The oxidation or reduction treatment can significantly impact the molecular structure of the supported metal catalyst and further affect the catalytic performance. With increasing pretreatment temperature (400–700 °C), the physicochemical properties, molecular structures, and electronic structures of 5.3 NiO_x/CeO_2 catalysts were investigated by various characterizations, such as BET, ICP/OES, Raman, XPS, and XRD. Based on BET results (Table 1), it was observed that introducing NiO_x species and pretreatment with increasing temperature caused collapsing of the small pores and agglomeration of CeO_2, resulting in decreased SSA and pore volume as well as increased pore diameter. Z. Wang *et al.* reported that the decreased specific surface area and increased pore diameter of synthesized transition metal (Co, Mn, Fe, Cr, and Ni) doped ceria substrate catalysts might be due to the sintering of the samples, resulting in larger crystalline grains with increasing calcination temperature.[48] Visible and UV Raman results proved that the concentrations of oxygen vacancies and defect ratio decreased with increasing pretreatment temperature. From the UV Raman spectra (Fig. 5) of both oxidized and reduced samples, 400 °C and 500 °C samples showed relatively similar peak intensities of the D-band (~600 cm^{-1}), while there is a large decrease in peak intensity of the D-band for 700 °C treated samples. These results were consistent with the results of BET (decreased SSA, increased pore size), indicating that significant molecular structure changes occurred after high temperature pretreatment at 700 °C. Overall, the oxidized 5.3 NiO_x/CeO_2 samples showed higher concentration and defect ratio than those of reduced samples at corresponding pretreatment temperatures (Table 2). Recently, C. Yang *et al.* reviewed the defect chemistry in CeO_2-based heterogeneous catalysis, and

Table 5 The peak assignments of the DRIFTS spectra

IR wavenumber (cm^{-1})	Assignments	Structure	Ref.
1010	Bridging bidentate nitrate, bidentate nitrate	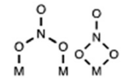	39 and 40
1227–1308	Monodentate nitrate, linear nitrite	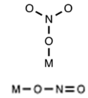	39 and 40
1241	Monodentate nitrate	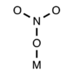	41 and 42
1267	Bidentate carbonate	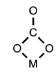	43–45
1338–1420	Monodentate carbonate	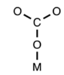	43–45
1467	Bidentate carbonate, monodentate nitrate	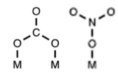	43–45
1535–1608	Bridging nitro, bridging bidentate nitrate	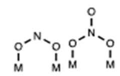	39 and 40
1806–1966	NO (gas phase)	N═O	39 and 40
1820–1833	NO adsorbed on Ni^{2+} or Ni^{+}	Ni^{n+}–NO	47
1990	CO adsorbed on Ni^{+}	Ni^{2+}–CO	47
2100–2200	CO (gas phase)	C≡O	43 and 46
2173–2193	CO adsorbed on Ni^{2+}	Ni^{2+}–CO	47
2175–2260	N_2O	O–N≡N	8
2295–2489	CO_2	O═C═O	46

the author claimed that these defect structures of CeO_2 play a key role in several catalytic activities.[49] The author also introduced several strategies for introducing defects, such as metal doping, chemical reduction, size and morphology control, and X-ray or electron beam irradiation. From Visible and UV Raman results, we can possibly obtain information on the concentration of oxygen vacancies/defect sites of oxidized and reduced catalysts, which can affect the catalytic performance. In addition to defect ratio changes, visible Raman results showed that the peak position of F_{2g} was slightly shifted (blue shift, 461 to 468 cm^{-1} (Oxi) and 469 cm^{-1} (Red)), which might be due to the disorder of oxygen species in the lattice, increasing particle size, and deficiency of Ce^{3+} species with increasing pretreatment temperature.[3,49,50]

The surface characteristics of the synthesized catalysts were inferred based on the XPS results. Notably, both oxidized and reduced catalysts exhibited different trends in response to varying heat treatment temperatures. For the oxidized catalyst, there was no significant difference in the Ce^{3+} ratio between treatments at 400 and 500 °C. However, in the case of reduced catalysts, the Ce^{3+} ratio decreased as the reduction temperature increased from 400 °C to 500 °C, suggesting that, during heat treatment under reducing conditions, a significant reduction of ceria did not occur. Samples treated at 700 °C exhibited similar Ce^{3+} ratios in both oxidation (18%) and reduction (19%) processes. In the case of samples subjected to oxidation, the change in the Ni^{3+} ratio was not significant on heating from 400 to 500 °C, compared to samples subjected to reduction, which clearly exhibited an increase in the Ni^{3+} ratio at both 400 and 500 °C. This observation is likely due to the formation of NiOOH or Ni vacancies, which lead to the presence of Ni^{3+}.[51] Based on the results, it can be inferred that the introduced OH adsorbed on the nickel oxide surface, resulting in the formation of hydroxyl groups (NiOOH), leading to an increase in Ni^{3+} content. However, at 700 °C, an increase in the amount of Ni existing as Ni^{3+} was observed in both the oxidized and reduced samples, although it is not as pronounced. This suggests that the influence of Ni vacancies due to high-temperature treatment might play a role. In this experiment, it is evident that both nickel vacancies and NiOOH did not significantly impact the CO oxidation reaction (Fig. 1 and 2). The O″ to O′ transition in the oxidized sample remains similar at 400 and 500 °C but decreases at 700 °C. This could be attributed to the disappearance of surface OH groups and the reduction of oxygen vacancies. The Raman results indicate a noticeable reduction in oxygen vacancies, suggesting a stronger correlation with the decrease in the O″ ratio as observed in the XPS results. For samples subjected to reduction, an increase in surface hydroxyl groups due to the introduction of OH in the process led to an observed increase in the Ni^{3+} ratio. However, in contrast, the O″ ratio decreased, indicating a reduction in oxygen vacancies that exceeds the increase in hydroxyl groups.

Moreover, at 700 °C, while the O″ ratio decreased significantly, the Ce^{3+} ratio did not decrease as significantly. This implies that the reduction in O″ is mostly due to a decrease in hydroxyl groups.

It was observed that XRD results showed the NiO peaks only in the oxidized samples, although the 700 °C sample showed a weak NiO peak intensity due to the low Ni wt% (*i.e.*, 3.9 wt%). In the case of the 400 °C and 500 °C treated samples, although Ni wt% was very similar (*i.e.*, 9.9 and 9.4 wt%, respectively), 5.3 NiO_x/CeO_2-500Oxi sample's NiO peak intensity was much higher than that of the 5.3 NiO_x/CeO_2-400Oxi sample. The results indicate that the formation of NiO is directly related to the calcination temperature. For reduced samples, the 400 °C treated sample contained both NiO and metallic Ni peaks, indicating that 400 °C was not enough to transfer NiO to Ni under the current experimental conditions. In the case of the 500 °C and 700 °C reduced samples, Ni was the dominant species, while the intensity of the 5.3 NiO_x/CeO_2-700R sample was weak due to the lower concentration of nickel particles. Although the XRD is a bulk technique, the results clearly provided evidence of the change in the oxidation state of surface NiO_x from Ni^{2+} to Ni^0. In addition to the BET and Raman spectroscopy results, the XRD also proved that the crystallinity and crystallite size of CeO_2 were dependent on the pretreatment temperature. For instance, the XRD peak intensity of CeO_2 increased and became sharpened with increasing pretreatment temperature due to the sintering or agglomeration of CeO_2 under high temperatures (Table 4).

4.2 Pretreatment effect on catalytic activity

As discussed above, the pretreatment conditions (oxidation and reduction) led to a change in molecular structures and textural properties for both the support (*i.e.*, CeO_2) and supported catalysts (*i.e.*, NiO_x/CeO_2). From the catalytic activity results (Fig. 1 and 2), it was shown that the lower temperature (*i.e.*, 400 °C and 500 °C) pretreated samples showed a better catalytic performance compared to the higher temperature pretreated samples (*i.e.*, 700 °C). When comparing Fig. 1 and 2, it was also observed that the oxidized samples showed slightly higher catalytic performance than the reduced samples. These results indicate that the catalytic performance of pretreated 5.3 NiO_x/CeO_2 catalysts was not only directly affected by the temperature but also related to the gas composition for the pretreatment procedures. In the case of the N_2O and N_2 formation (or products' selectivity), the chemical reactions of N_2O formation and decomposition could be related: (1) $2NO + CO \rightarrow N_2O + CO_2$ ($\Delta H_r^0 = -381.45$ kJ), (2) $N_2O + CO \rightarrow N_2 + CO_2$ ($\Delta H_r^0 = -365.05$ kJ).[40,52,53] Based on thermodynamic values, the N_2O formation could be the favourable step compared to N_2O decomposition for the N_2 formation. Although the non-catalytic reaction is different from the catalytic reaction, the thermodynamic values and product formation are well matched with the current experimental results (Fig. 1(c)–(d) and 2(c)–(d)). It should be noted that N_2 and N_2O could be formed through different reaction pathways: $2NO \rightarrow N_2 + O_2$ ($\Delta H_r^0 = -180.5$ kJ), $2NO \rightarrow N_2O + 0.5O_2$ ($\Delta H_r^0 = -98.45$ kJ), $2N_2O \rightarrow 2N_2 + 2O_2$ ($\Delta H_r^0 = -164.1$ kJ). However, these reactions are thermodynamically unfavourable compared to the two step mechanisms. Two step mechanisms over diverse catalysts (*i.e.*, solid solution, supported catalysts) have been reported for the NO reduction by CO. X. Yao *et al.* reported that adsorbed NO (or NO_x) on $Ce_{0.67}Sn_{0.33}O_2$ produced the N_2O/N_2 mixture at a lower temperature (~200 °C) and considerable N_2 production at a higher temperature (250–400 °C). The authors hypothesized that oxygen vacancies and Ce^{3+} surfaces increase the NO dissociation and the CO adsorption, respectively, at higher temperatures, increasing N_2 and CO_2 production.[54] X. Zhang *et al.* and Sugi *et al.* also observed the N_2O formation at lower temperatures or the early stages at a fixed reaction temperature (*i.e.*, 200 °C) over $CuO_x/CeO_2–Fe_2O_3$ and Fe_2O_3/SiC catalysts, respectively. The authors suggested that at high temperatures, the N_2O reduced to N_2 instead of being displaced by NO.[55,56]

The N_2O decomposition temperature (or N_2 formation) was affected by the pretreatment conditions, especially under the high temperature reducing conditions. The N_2O decomposition temperature over the 5.3 NiO_x/CeO_2-700R catalyst was much higher than that of other samples. It is worthwhile to note that the NO or CO conversion and N_2 selectivity of 5.3 NiO_x/CeO_2-700R did not reach 100% up to 500 °C (62% for NO conversion, 44% for CO conversion, and 37% for N_2 selectivity at 500 °C). It might be deduced that the decreased catalytic activity can be influenced by a combination of the relatively lower concentration of Ni species (1.4%), lower specific surface area (22 $m^2\ g^{-1}$), and lower concentration of oxygen vacancies ($0.49 \times 10^{21}\ cm^{-3}$) compared to other samples even fixing at the same surface density (5.3 Ni per nm^2). Furthermore, it was reported

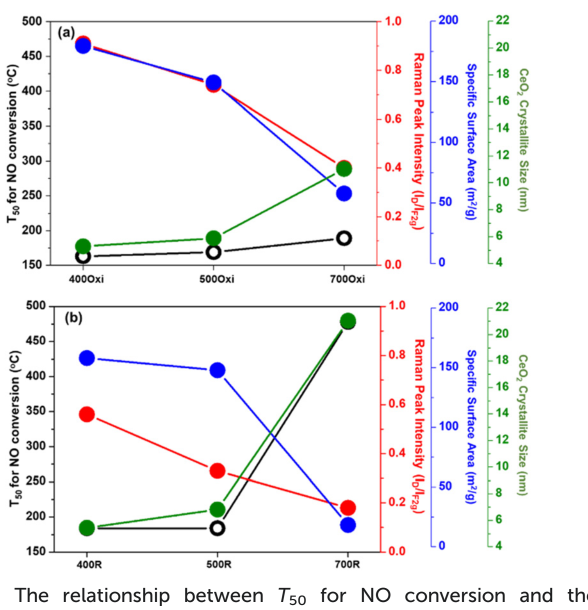

Fig. 9 The relationship between T_{50} for NO conversion and the physical properties of (a) oxidized and (b) reduced 5.3 NiO_x/CeO_2 catalysts.

that surface oxygen vacancies can promote N_2O dissociation.[57] In this respect, the low oxygen vacancy concentration (low $I_D/I_{F_{2g}}$) of the reduced 5.3 Ni/CeO_2-700R sample might interrupt the second step of the reaction mechanism (N_2O dissociation by CO). The relationship between catalytic performance (T_{50} for NO conversion) and physical properties (Raman peak intensity ($I_D/I_{F_{2g}}$), specific surface area, and CeO_2 crystallite size) of the catalysts are shown in Fig. 9. For both oxidized and reduced catalysts, the T_{50} value was increased (decreasing catalytic performance) with decreasing defect ratio ($I_D/I_{F_{2g}}$) and SSA as well as increasing CeO_2 crystallite size, indicating that the catalytic performance of catalysts was mainly affected by the physicochemical properties (oxygen vacancies/defect sites, SSA, oxidation state of Ni) at a fixed surface density of nickel (Ni atoms per nm^2). The results based on NO reduction by CO using various materials, supports, and synthesis methods reported in the literature are summarized in Table S1† (based on T_{50} for the NO conversion ($T_{50,NO}$) and T_{50} for the CO conversion ($T_{50,CO}$)). $T_{50,NO}$ ranged from 102 °C to 498 °C, and $T_{50,CO}$ varied from 142 °C to 470 °C. The synthesis method also significantly influenced the activity, but from the perspective of materials, catalysts with CeO_2-based materials as the support showed lower T_{50} (Pd/$CeZrO_2$, $T_{50,NO}$ = 102 °C), and CuO as the active material generally achieved lower T_{50} (CuO/CeO_2, $T_{50,NO}$ = 125 °C). In contrast, catalysts using TiO_2 or Al_2O_3 as supports typically showed higher T_{50} (Pd/Al_2O_3, $T_{50,NO}$ = 279 °C, CuO/TiO_2, $T_{50,NO}$ = 290 °C). In this work, the prepared catalyst, 5.3 NiO_x/CeO_2-400Oxi, achieved relatively low $T_{50,NO}$ (167 °C) and $T_{50,CO}$ (175 °C).

4.3 Reaction mechanism of NO reduction by CO

Based on the physicochemical characterization results and *in situ* DRIFTS, a possible reaction mechanism for NO reduction by CO could be proposed for both catalysts, 5.3 NiO_x/CeO_2-400Oxi and 5.3 NiO_x/CeO_2-700R (Fig. 10). Taking the 5.3 NiO_x/CeO_2-400Oxi catalyst as an example, at low temperatures, rather than CO, NO is mainly adsorbed as nitrate or nitrite species owing to the unpaired electron of NO. Then, as the temperature gradually increases to 220 °C, the adsorbed NO gradually undergoes desorption, decomposition, and transformation into N_2O and N_2. At the same time, small amounts of CO are also adsorbed on the catalytic surface at low temperatures, and as the temperature increases, CO adsorption becomes more significant. Adsorbed CO reduces the surface of the catalyst ($Ce^{4+} \rightarrow Ce^{3+}$), resulting in more surface oxygen vacancies. Increasing the presence of surface Ce^{3+} facilitates additional adsorption sites for the CO_x species (CO and CO_2), which, in turn, weakens the N–O bond and enhances the dissociation of NO_x. According to widely accepted studies,[40,57] surface Ce^{3+} plays a crucial role in facilitating the adsorption of CO species. Xiong *et al.* indicated that the dissociation of NO is a critical step in the NO + CO reaction, and the presence of oxygen vacancies weakens the N–O bonds, promoting their dissociation.[58] Additionally, Yao *et al.* demonstrated that surface oxygen vacancies contribute significantly to the dissociation of N_2O.[54] Consequently, this promotes the formation of N_2 and CO_2 as the end products from 190 °C. It is expected that the reaction mechanism of 5.3 NiO_x/CeO_2-700R is similar to that of 5.3 NiO_x/CeO_2-400Oxi. However, the reaction is expected to occur at a higher temperature. This is likely attributed to differences in the catalyst's physicochemical properties, such as lower surface area and fewer oxygen vacancies in 5.3 NiO_x/CeO_2-700R compared to 5.3 NiO_x/CeO_2-400Oxi.

5. Conclusions

In this study, CeO_2 support materials were firstly pretreated under oxidation and reduction conditions at different

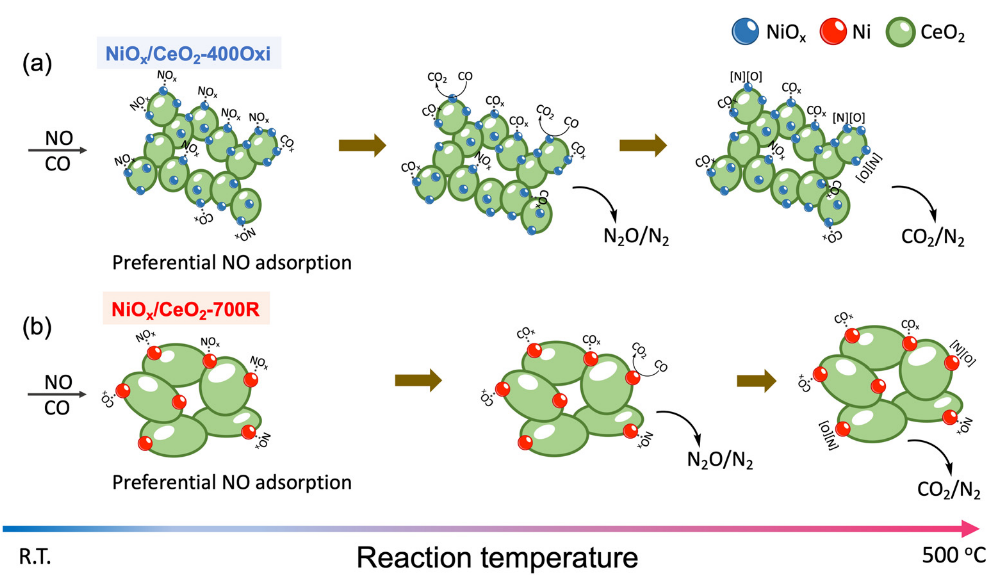

Fig. 10 A possible reaction mechanism for the NO reduction by CO over (a) NiO_x/CeO_2-400Oxi and (b) NiO_x/CeO_2-700R. The yellow spheres indicate NiO_x and the red spheres indicate Ni.

temperatures (*i.e.*, 400, 500, and 700 °C). The NiO_x supported on the pretreated CeO_2 catalysts were synthesized at the same conditions that were used for the CeO_2 support with a surface density of 5.3 Ni per nm^2. ICP/OES results confirmed that the Ni wt% and SD values were similar to the target values calculated using the synthesized sample's SSA. Afterwards, the NO reduction by CO over synthesized catalysts was investigated to understand the relationship between catalyst synthesis conditions and the catalytic activity. From BET (Table 1) and XRD (Fig. 7) results, it was clearly shown that the increased pretreatment temperature led to the formation of NiO (oxidation) and metallic Ni species (reduction), decreased SSA and increased crystallite size of the CeO_2 support. The Visible and UV Raman (Fig. 4 and 5) results proved that the concentration of oxygen vacancies and defect sites, crucial to enhancing the catalytic activity, decreased with increasing pretreatment temperature. The XPS results provided information about the oxidation state of the catalyst's surface, indicating the concentration of oxygen vacancies. Consistent with the Raman results, it was observed that as the pretreatment temperature increased, the concentration of oxygen vacancies decreased. The catalytic activity of both oxidized and reduced NiO_x/CeO_2 catalysts decreased with increasing pretreatment temperature, while the oxidized catalysts showed slightly higher activity than reduced samples. From *in situ* DRIFTS results, NO-based surface species were mainly adsorbed on the active sites (Ni^+ or Ni^{2+}) at lower temperatures (<250 °C), then were converted to N_2O species by means of exposing CO at 200–250 °C. After the N_2O intermediate species was formed, CO-based surface species occupied the surface of active sites. Finally, N_2O could be further reduced to N_2 and formed Ni–NO (or Ni–CO) at higher temperatures (>200 °C). CO_2 was produced through the carbonate species formation and decomposition on the catalyst surface that was pre-occupied by NO dominantly. Based on physicochemical and activity results, it can be concluded that the catalytic activity of pretreated NiO_x/CeO_2 catalysts was mainly controlled by the physical properties of the catalysts.

Author contributions

K. Lee: methodology, formal analysis, writing – original draft, writing – review & editing, B. Kim: formal analysis, writing – original draft, writing – review & editing, J. Lee: formal analysis, writing – review & editing, G. Kwon: formal analysis, writing – review & editing, K. Yoon: formal analysis, H. Song: formal analysis, K. Min: formal analysis, S. Shim: funding acquisition, S. Hwang: funding acquisition, T. Kim: supervision, writing – original draft, writing – review & editing, project administration, funding acquisition. All authors have given approval to the final version of the manuscript.

Conflicts of interest

There are no conflicts of interest to declare.

Acknowledgements

The authors acknowledge funding support from the National Science Foundation (NSF-CBET-2050824). The authors would also like to thank the Advanced Energy Research and Technology Center (AERTC) for the facilities at Stony Brook University. This research used the beamline 28-ID-1 of the National Synchrotron Light Source II (NSLS-II), which is the U.S. Department of Energy (DOE) Office of Science User Facilities at Brookhaven National Laboratory under Contract No. DE-SC0012704. This research was supported by the MOTIE (Ministry of Trade, Industry, and Energy) in Korea, under the Human Resource Development Program for Industrial Innovation (Global) (P0017303, Smart Manufacturing Global Talent Training Program) supervised by the Korea Institute for Advancement of Technology (KIAT).

References

1 G. Zhiming, D. Qianzi, M. Hongwei and L. Zhanping, *J. Rare Earths*, 2016, **34**, 1213–1220.
2 E. D. Arabaci, A. M. Önal and S. Özkar, *J. Electrochem. Soc.*, 2020, **167**, 106513.
3 L. He, B. Liang, L. Li, X. Yang, Y. Huang, A. Wang, X. Wang and T. Zhang, *ACS Catal.*, 2015, **5**, 1623–1628.
4 W. Zou, C. Ge, M. Lu, S. Wu, Y. Wang, J. Sun, Y. Pu, C. Tang, F. Gao and L. Dong, *RSC Adv.*, 2015, **5**, 98335–98343.
5 Z. Liu, S. Yao, A. Johnston-Peck, W. Xu, J. A. Rodriguez and S. D. Senanayake, *Catal. Today*, 2018, **311**, 74–80.
6 X. Du, D. Zhang, L. Shi, R. Gao and J. Zhang, *J. Phys. Chem. C*, 2012, **116**, 10009–10016.
7 Y. Wang, A. Zhu, Y. Zhang, C. Au, X. Yang and C. Shi, *Appl. Catal., B*, 2008, **81**, 141–149.
8 X. Cheng, A. Zhu, Y. Zhang, Y. Wang, C. Au and C. Shi, *Appl. Catal., B*, 2009, **90**, 395–404.
9 C. Tang, B. Sun, J. Sun, X. Hong, Y. Deng, F. Gao and L. Dong, *Catal. Today*, 2017, **281**, 575–582.
10 S. Zhang, J. Lee, D. H. Kim and T. Kim, *Catal. Sci. Technol.*, 2020, **10**, 2359–2368.
11 K.-M. Lee, G. Kwon, S. Hwang, J. A. Boscoboinik and T. Kim, *Catal. Sci. Technol.*, 2021, **11**, 7850–7865.
12 R. L. Martins and M. Schmal, *J. Braz. Chem. Soc.*, 2014, **25**, 2399–2408.
13 E. Mamontov, T. Egami, R. Brezny, M. Koranne and S. Tyagi, *J. Phys. Chem. B*, 2000, **104**, 11110–11116.
14 P. Snytnikov, M. Popova, Y. Men, E. Rebrov, G. Kolb, V. Hessel, J. Schouten and V. Sobyanin, *Appl. Catal., A*, 2008, **350**, 53–62.
15 S. Zhang, Y. Li, J. Huang, J. Lee, D. H. Kim, A. I. Frenkel and T. Kim, *J. Phys. Chem. C*, 2019, **123**, 7166–7177.
16 I. Iglesias, A. Quindimil, F. Marino, U. De-La-Torre and J. R. González-Velasco, *Int. J. Hydrogen Energy*, 2019, **44**, 1710–1719.
17 C. A. Roberts, D. Prieto-Centurion, Y. Nagai, Y. F. Nishimura, R. D. Desautels, J. Van Lierop, P. T. Fanson and J. M. Notestein, *J. Phys. Chem. C*, 2015, **119**, 4224–4234.

18 T. C. Peck, G. K. Reddy, M. Jones and C. A. Roberts, *J. Phys. Chem. C*, 2017, **121**, 8435–8443.
19 T. C. Peck, G. K. Reddy and C. A. Roberts, *Catal. Sci. Technol.*, 2019, **9**, 1132–1140.
20 T. Kim, A. Burrows, C. J. Kiely and I. E. Wachs, *J. Catal.*, 2007, **246**, 370–381.
21 S. Vivek, S. Preethi, T. V. Kumar, A. K. Sundramoorthy and K. S. Babu, *J. Alloys Compd.*, 2020, **816**, 152608.
22 C. Wu, Z. Xiao, L. Wang, G. Li, X. Zhang and L. Wang, *Catal. Sci. Technol.*, 2021, **11**, 1965–1973.
23 S. D. Senanayake, J. Evans, S. Agnoli, L. Barrio, T.-L. Chen, J. Hrbek and J. A. Rodriguez, *Top. Catal.*, 2011, **54**, 34–41.
24 J. Carrasco, L. Barrio, P. Liu, J. A. Rodriguez and M. V. Ganduglia-Pirovano, *J. Phys. Chem. C*, 2013, **117**, 8241–8250.
25 T. Xu, J. Xue, X. Zhang, G. He and H. Chen, *Appl. Surf. Sci.*, 2017, **402**, 294–300.
26 J. Taghavimoghaddam, G. P. Knowles and A. L. Chaffee, *J. Mol. Catal. A: Chem.*, 2012, **358**, 79–88.
27 M. Daniel and S. Loridant, *J. Raman Spectrosc.*, 2012, **43**, 1312–1319.
28 I. Kosacki, T. Suzuki, H. U. Anderson and P. Colomban, *Solid State Ionics*, 2002, **149**, 99–105.
29 J. E. Spanier, R. D. Robinson, F. Zhang, S.-W. Chan and I. P. Herman, *Phys. Rev. B: Condens. Matter Mater. Phys.*, 2001, **64**, 245407.
30 W. Weber, K. Hass and J. McBride, *Phys. Rev. B: Condens. Matter Mater. Phys.*, 1993, **48**, 178.
31 T. Taniguchi, T. Watanabe, N. Sugiyama, A. Subramani, H. Wagata, N. Matsushita and M. Yoshimura, *J. Phys. Chem. C*, 2009, **113**, 19789–19793.
32 M.-F. Luo, Z.-L. Yan, L.-Y. Jin and M. He, *J. Phys. Chem. B*, 2006, **110**, 13068–13071.
33 Z. Wu, M. Li, J. Howe, H. M. Meyer III and S. H. Overbury, *Langmuir*, 2010, **26**, 16595–16606.
34 T. Livneh and E. Sterer, *Phys. Rev. B: Condens. Matter Mater. Phys.*, 2006, **73**, 085118.
35 K.-M. Lee, M. Brito, J. DeCoster, K. Linskens, K. Mehdi, W.-I. Lee, E. Kim, H. Kim, G. Kwon, C.-Y. Nam and T. Kim, *Mol. Catal.*, 2022, **528**, 112465.
36 C. Deng, Q. Huang, X. Zhu, Q. Hu, W. Su, J. Qian, L. Dong, B. Li, M. Fan and C. Liang, *Appl. Surf. Sci.*, 2016, **389**, 1033–1049.
37 L. Atzori, M. G. Cutrufello, D. Meloni, B. Onida, D. Gazzoli, A. Ardu, R. Monaci, M. F. Sini and E. Rombi, *Front. Chem. Sci. Eng.*, 2021, **15**, 251–268.
38 N. Jayababu, M. Poloju, J. Shruthi and M. R. Reddy, *RSC Adv.*, 2019, **9**, 13765–13775.
39 L. Liu, B. Liu, L. Dong, J. Zhu, H. Wan, K. Sun, B. Zhao, H. Zhu, L. Dong and Y. Chen, *Appl. Catal., B*, 2009, **90**, 578–586.
40 C. Deng, M. Li, J. Qian, Q. Hu, M. Huang, Q. Lin, Y. Ruan, L. Dong, B. Li and M. Fan, *Chem. - Asian J.*, 2016, **11**, 2144–2156.
41 X. Zhang, H. He, H. Gao and Y. Yu, *Spectrochim. Acta, Part A*, 2008, **71**, 1446–1451.
42 X. Dai, W. Jiang, W. Wang, X. Weng, Y. Shang, Y. Xue and Z. Wu, *Chin. J. Catal.*, 2018, **39**, 728–735.
43 N. Liu, X. Chen, J. Zhang and J. W. Schwank, *Catal. Today*, 2015, **258**, 139–147.
44 L. Zhang, X. Yao, Y. Lu, C. Sun, C. Tang, F. Gao and L. Dong, *J. Colloid Interface Sci.*, 2018, **509**, 334–345.
45 S. Gaur, H. Wu, G. G. Stanley, K. More, C. S. Kumar and J. J. Spivey, *Catal. Today*, 2013, **208**, 72–81.
46 X. Cheng, Y. Cheng, Z. Wang and C. Ma, *Fuel*, 2018, **214**, 230–241.
47 M. Mihaylov, K. Chakarova and K. Hadjiivanov, *J. Catal.*, 2004, **228**, 273–281.
48 Z. Wang, F. Lin, S. Jiang, K. Qiu, M. Kuang, R. Whiddon and K. Cen, *Fuel*, 2016, **166**, 352–360.
49 C. Yang, Y. Lu, L. Zhang, Z. Kong, T. Yang, L. Tao, Y. Zou and S. Wang, *Small Struct.*, 2021, **2**, 2100058.
50 T. Hattori, K. Kobayashi and M. Ozawa, *Jpn. J. Appl. Phys.*, 2016, **56**, 01AE06.
51 A. P. Grosvenor, M. C. Biesinger, R. S. C. Smart and N. S. McIntyre, *Surf. Sci.*, 2006, **600**, 1771–1779.
52 D. Prieur, W. Bonani, K. Popa, O. Walter, K. W. Kriegsman, M. H. Engelhard, X. Guo, R. Eloirdi, T. Gouder and A. Beck, *Inorg. Chem.*, 2020, **59**, 5760–5767.
53 L. Xue, C. Zhang, H. He and Y. Teraoka, *Appl. Catal., B*, 2007, **75**, 167–174.
54 X. Yao, C. Tang, Z. Ji, Y. Dai, Y. Cao, F. Gao, L. Dong and Y. Chen, *Catal. Sci. Technol.*, 2013, **3**, 688–698.
55 X. Zhang, X. Cheng, C. Ma and Z. Wang, *Catal. Sci. Technol.*, 2018, **8**, 3336–3345.
56 Y. Sugi, N. Todo and T. Sato, *Bull. Chem. Soc. Jpn.*, 1975, **48**, 337–338.
57 X. Yao, Q. Yu, Z. Ji, Y. Lv, Y. Cao, C. Tang, F. Gao, L. Dong and Y. Chen, *Appl. Catal., B*, 2013, **130**, 293–304.
58 Y. Xiong, X. Yao, C. Tang, L. Zhang, Y. Cao, Y. Deng, F. Gao and L. Dong, *Catal. Sci. Technol.*, 2014, **4**, 4416–4425.